Synthesis and properties of highly mismatched II–O–VI alloys

K.M. Yu, W. Walukiewicz, M.A. Scarpulla, O.D. Dubon, W. Shan, J. Wu, J.W. Beeman and P. Becla

Abstract: Ternary and quaternary dilute II–VI oxides were synthesised using a highly non-equilibrium method: the combination of O ion implantation and pulsed-laser melting. CdO_xTe_{1-x} thin films have been produced with x up to 0.015 and with the energy gap reduced by 0.15 eV. Optical transitions corresponding to both the lower (E_-) and upper (E_+) conduction sub-bands, resulting from the anticrossing interaction between the localised O states and the extended conduction states of the matrix, are clearly observed in quaternary $Cd_{0.6}Mn_{0.4}O_xTe_{1-x}$ and $Zn_{0.88}Mn_{0.12}O_xTe_{1-x}$ layers. These results have important implications for the existing theoretical models of the electronic structure of the highly mismatched alloys. In $Zn_{1-x}Mn_xTe$, where the O level lies below the conduction band edge, it was demonstrated that incorporation of a small amount of oxygen leads to the formation of a narrow, oxygen-derived band of extended states located well below the conduction band edge of the ZnMnTe matrix. The three absorption edges of this material (~0.73, 1.83 and 2.56 eV) cover the entire solar spectrum providing a material envisioned for multiband, single-junction, high-efficiency photovoltaic devices.

1 Introduction

Group II–O–VI semiconductors with the anions partially replaced by highly electronegative isoelectronic O atoms are a direct analogue of the extensively studied dilute nitrides. It has been suggested and experimentally demonstrated that the electronic band structure of such highly mismatched alloys (HMAs) is determined by the anticrossing interaction between localised O or N states and the extended states of the semiconductor matrix [1–4]. The interaction splits the conduction band into two nonparabolic sub-bands, E_+ and E_-. The large modification of the electronic band structure profoundly affects the optical and electrical properties of these alloys. In GaN_xAs_{1-x} HMAs, it has been shown that incorporation of a small amount of N leads to a large reduction of the fundamental bandgap ([1], and for a review see [5]), increase of the electron effective mass [6], improved donor activation efficiency of the group-VI donors [7, 8] and the mutual passivation of the group-IV donors and the nitrogen [8–12]. Although similar or even more pronounced effects are also expected in II–O–VI HMAs [2], much less work has been done on these materials because of the difficulties in the synthesis of the alloys with large enough O content [13, 14].

The anticrossing interaction between the extended conduction-band states of a semiconductor matrix and the highly localised electronic states introduced by the isoelectronic substitutional atoms with high electronegativity, such as N in GaAs or O in ZnSe, can be expressed as [1–4]

$$E_\pm(k) = \frac{1}{2}\left\{(E_M(k) + E_L) \pm \sqrt{(E_M(k) - E_L)^2 + 4V^2}\right\} \tag{1}$$

where $E_M(k)$ and E_L are the energies of the unperturbed conduction band and of the localised states (E_O for oxygen and E_N for N) relative to the top of the valence band, respectively. The matrix element describing the interaction and hybridisation between the localised states and the extended conduction band states $V = C_{LM}x^{1/2}$, where C_{ML} is a constant dependent on the semiconductor matrix (C_{NM} for N in III–V and C_{OM} for O in II–VI) and x is the alloy composition. The energy positions of the sub-band edges given by (1) depend on the interaction parameter V and the location of E_L with respect to the conduction band edge E_M. The interaction between the localised isoelectronic states and the extended conduction-band states has a drastic effect on the dispersion relation of the two conduction sub-bands E_- and E_+. When the localised state is located within the conduction band of the matrix (e.g. O in CdTe and N in GaAs), the conduction-band states associated with the E_- edge retain the extended E_M-like character and those at the E_+ edge have a more localised E_O-like character. This is depicted in Fig. 1*a*. However, when the localised states lie below the conduction-band edge as shown in Fig. 1*b*, the conduction sub-band edges of E_- and E_+ switch character; the E_- sub-band states are of a highly localised character and the E_+ sub-band states become more extended. This latter situation occurs for O in ZnTe, MnTe, MgTe and $Cd_{1-y}Mn_yTe$ with $y \geq 0.4$.

Using O^+-implantation in $Cd_{1-y}Mn_yTe$ substrates followed by rapid thermal annealing (RTA), we reported for the first time successful formation of $Cd_{1-y}Mn_yO_xTe_{1-x}$ alloys with x up to 0.004, corresponding to an activation

IEE Proceedings online no. 20040932

doi: 10.1049/ip-opt:20040932

Paper received 30th April 2004

K.M. Yu, W. Walukiewicz, W. Shan, J. Wu and J.W. Beeman are with the Materials Sciences Division, Lawrence Berkeley National Laboratory, Berkeley, CA 94720, USA

M.A. Scarpulla and O.D. Dubon are with the Materials Sciences Division, Lawrence Berkeley National Laboratory, and the Department of Materials Science and Engineering, University of California, Berkeley, CA 94720, USA

P. Becla is with the Department of Materials Science and Engineering, Massachusetts Institute of Technology, Cambridge, MA 02139, USA

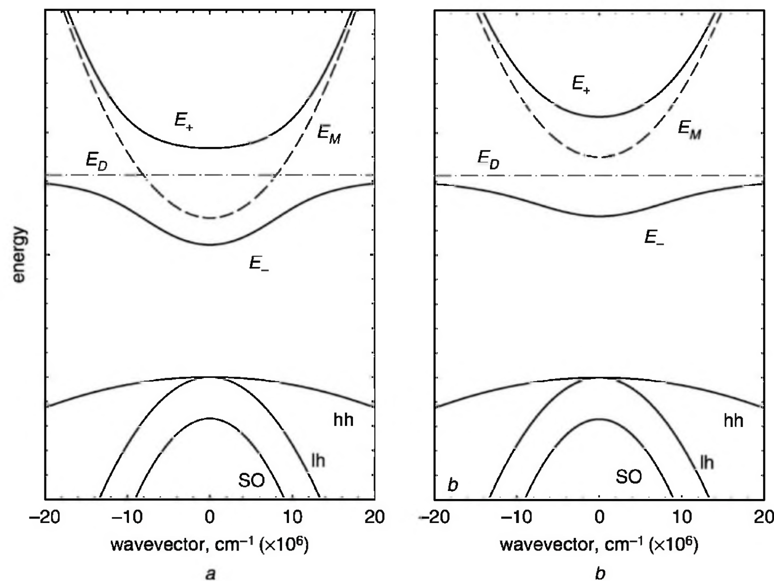

Fig. 1 *Schematic illustrations of the effects of band anticrossing on the Γ conduction band structure*

a Highly electronegative isoelectronic impurity-induced localised state resonant with the conduction band
b Localised state located below the conduction band
Solid lines are restructured E_- and E_+ sub-bands resulting from band anticrossing interaction between the localised states (dash-dotted line) and the extended states of the conduction band (broken line)

efficiency of O of $<10\%$ [15]. Even for such a small amount of O incorporated in the group-VI sublattice, a bandgap reduction in the range of ~70 meV (for low y) was reported. In order to synthesise II–O–VI alloys with high O content, a more highly non-equilibrium synthesis means is needed.

Pulsed-laser melting (PLM) utilising an excimer laser with pulse width of ~20–50 ns is a highly non-equilibrium processing technique that was developed and extensively investigated in the 1970s and 1980s [16, 17]. It involves the absorption of laser radiation, melting of the implant-damaged or amorphised layer, and its subsequent rapid epitaxial regrowth. Epitaxy is seeded at the solid–liquid interface by the crystalline bulk in a manner very similar to liquid phase epitaxy (LPE), but with the whole process occurring on a much shorter time scale, typically between 10^{-8} and 10^{-6} s. It was shown that using the PLM method, amorphous layers of GaAs formed by high-dose implantation can be regrown into nearly perfect single crystals with electrical activities of dopants well above those achievable by furnace annealing [17]. This technique appears to be well suited for the synthesis of highly mismatched alloys.

Recently, we demonstrated that PLM followed by RTA greatly enhanced incorporation of substitutional N in N^+-implanted GaAs [18, 19]. Films implanted with 1.8% N exhibited a fundamental bandgap of 1.26 eV (a bandgap reduction of 160 meV), corresponding to an N activation efficiency of 50%. The optical and crystalline quality of the synthesised film is comparable to GaN_xAs_{1-x} thin films of similar composition grown by epitaxial growth techniques. Compared to films produced by N^+ implantation and rapid thermal annealing only, the introduction of pulsed-laser annealing improved N incorporation by a factor of five [20]. In addition to GaN_xAs_{1-x}, synthesis of diluted ferromagnetic $Ga_{1-x}Mn_xAs$ with Curie temperature as high as 130 K using the PLM process has recently been demonstrated ([21], and unpublished work by M.A. Scarpulla *et al.*).

In this paper, we review our work on the synthesis of the II–O–VI HMAs for cases when the localised state is located within and below the conduction band of the matrix, using ion implantation and pulsed-laser melting. Detailed optical studies of these alloys are presented. In particular, we discuss here the potential photovoltaic applications of the $Zn_{1-y}Mn_yO_xTe_{1-x}$ HMA that has a narrow band of extended states within a semiconductor bandgap. This material satisfies the criteria for a multiband semiconductor and can be used to test the theoretical predictions of enhanced efficiency in the intermediate band solar cell (IBSC) concept.

2 Experimental

Multiple energy implantation with 90 and 30 keV O ions was carried out on various II–VI single crystals to form ~0.2-μm-thick layers with relatively constant initial O concentrations, corresponding to O mole fractions of 0.01–0.04 (i.e. 1–4%). The O^+-implanted layers of the crystals were pulsed-laser melted in air using a KrF laser ($\lambda = 248$ nm) with a FWHM pulse duration of ~38 ns. After passing through a multi-prism homogeniser, the energy fluence at the sample was in the range 20–300 mJ/cm^2. Some of the samples were rapid thermally annealed after the PLM process at temperatures of 300–600 °C for 10 s (RTA) in flowing N_2.

The bandgap of the synthesised layers was measured using photomodulated reflectance (PR) spectroscopy at room temperature [22]. Radiation from a 300-W halogen tungsten lamp dispersed by a 0.5-m monochromator was focused on the samples as a probe beam. A chopped HeCd laser beam ($\lambda = 442$ nm or 325 nm) provided the photomodulation. PR signals were detected by a Si or Ge photodiode using a phase-sensitive lock-in amplification system. The values of the bandgap and the linewidth were determined by fitting the PR spectra to the Aspnes third-derivative functional form [23]. The effects of applied pressure on the E_- transition in the $Zn_{0.88}Mn_{0.12}O_xTe_{1-x}$ were studied in order to verify the origin of the E_- band. Application of hydrostatic pressure was accomplished by mounting small sample chips with sizes of ~$200 \times 200\ \mu m^2$ into gasketed diamond anvil cells while the optical

transitions in the samples were measured by photomodulated transmission (PT).

3 Results and discussion

3.1 II–O–VI alloys with E_O resonant with the conduction band

The conventional ion beam synthesis (IBS) technique, O^+ implantation followed by thermal annealing, was used as our first approach to form II–O–VI HMAs [15]. For O^+-implanted CdTe samples we found no optical transition for the as-implanted materials. This is attributed to the lattice damage due to the large O dose implanted in the CdTe. A distinct transition feature at around the CdTe bandgap (1.51 eV) is observed in O^+-implanted samples after RTA at temperatures higher than 300°C. The linewidth of the main transition improves as the RTA temperature increases due to the removal of implantation-induced crystalline defects in the samples. For all the CdTe samples implanted with O^+ followed by RTA, no significant bandgap reduction can be observed. This indicates that the implanted O does not reside in the Te sublattice, but possibly agglomerates to form O bubbles, similar to the case of N in N^+-implanted GaAs after RTA at temperatures higher than 950°C [24]. In CdTe crystals alloyed with >2% Mn ($Cd_{1-y}Mn_yTe$ with $y > 0.02$), small amounts of O up to $x \sim 0.004$ can be incorporated in the Te sublattice after 600°C 10 s RTA, causing a sizable decrease in the bandgap (~70 meV). The bandgap reduction increases with y; the largest value observed is 190 meV in O^+-implanted $Cd_{0.38}Mn_{0.62}Te$ [15].

Much enhanced bandgap reduction in O^+-implanted CdTe is observed when PLM is used as a post-implantation process instead of RTA. This is illustrated in the series of PR spectra in Fig. 2 from CdTe with implanted O doses corresponding to 0–4 mole % followed by PLM with an energy fluence of 40 mJ/cm^2. PR spectra from a CdTe substrate and an unimplanted CdTe sample treated with the

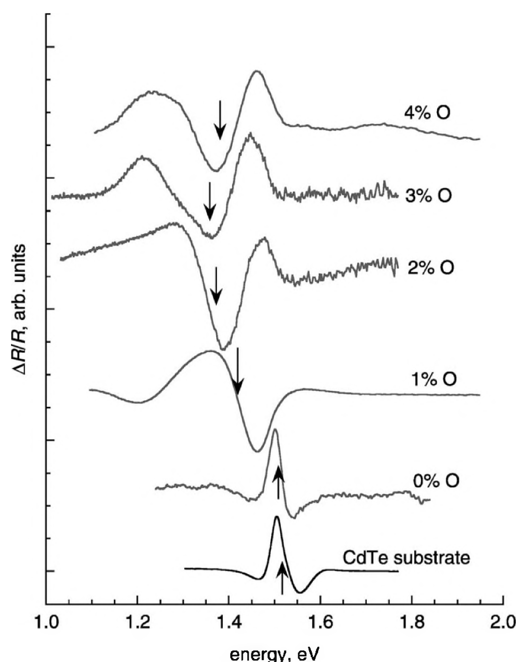

Fig. 2 *Photoreflectance spectra of O^+-implanted CdTe samples after PLM with energy fluence 40 mJ/cm^2*

Samples were implanted with O with total dose corresponding to 0–4 mole % of O in CdTe; bandgap values as determined by fitting the PR spectra to the Aspnes third-derivative functional form are indicated as arrows

PLM process (0% O) are also included for direct comparison. A large bandgap reduction (ΔE) is immediately evident in the O^+-implanted CdTe samples after PLM. For the CdTe sample implanted with 2% O after PLM, the fundamental gap is 1.37 eV, corresponding to a bandgap reduction $\Delta E = 140$ meV. This large reduction in the bandgap is a clear indication of O-incorporation in the Te sublattice, forming CdO_xTe_{1-x} alloys. Contrary to the case of PLM of N^+ -implanted GaAs, where an optical transition can only be observed after RTA following PLM [18, 19], O^+-implanted CdTe samples show clear, sharp optical transitions after PLM without additional thermal annealing. This can be attributed to the higher resistance of CdTe (and II–VI alloys in general) to the formation of structural defects due to the more ionic nature of the crystals.

Figure 2 also shows that the bandgap reduction (or O-incorporation) increases as the implanted O content increases from 1 to 2%. However, a further increase in the implanted O concentration leads to a saturation of the bandgap at ~1.37 eV. This suggests that there is a maximum in the amount of O that can be incorporated in the Te sublattice in CdTe under the present PLM conditions. Notice that there is no reduction in the bandgap energy for an unimplanted CdTe sample after PLM (0% O). This clearly shows that the bandgap reduction indeed arises from the O-incorporation in the Te sublattice, but not from the laser melting process.

It was mentioned earlier that in these HMAs, the anticrossing interaction between the localised states of O and the extended conduction band states of CdTe splits the conduction band into two nonparobolic sub-bands (E_- and E_+) [1–4]. The large reduction in the fundamental bandgap in CdO_xTe_{1-x} alloys is due to the optical transition from the valence band to the lower sub-band E_- (Fig. 1*a*). For all the CdO_xTe_{1-x} alloys synthesised by ion implantation and PLM, no transition from the valence band to the upper sub-band E_+ has been observed in our optical measurements. This can be explained by the fact that the E_+ sub-band edge in this case is formed from states of largely localised-like character. Since the dipole interaction for optical transitions couples much more strongly to extended states than localised ones, the transition related to E_+ is inherently weak.

Figure 3*a* summarises the bandgap energies of the CdO_xTe_{1-x} alloys formed by O^+-implantation in CdTe followed by PLM with laser energy fluence in the range 40–100 mJ/cm^2 as a function of the implanted O^+ concentration. We point out that no bandgap reduction is found in O^+-implanted CdTe followed by PLM with energy fluence lower than 30 mJ/cm^2, suggesting that under the present PLM conditions the melting threshold of CdTe is ~40 mJ/cm^2. This is in agreement with the recently reported melting threshold energy fluence for CdTe determined by time-resolved reflectivity (TRR) [25].

For O^+-implanted CdTe samples PLM at 40 and 60 mJ/cm^2, the bandgap follows a similar trend. It is reduced for the implanted O range from 1% to 2% and then it saturates at ~1.37 eV when more O atoms are introduced into the substrate. This saturation can be attributed to the O content exceeding the kinetic solubility limit even for the short melt duration of ~300 ns. However, the bandgap of samples melted at energy fluence higher than 60 mJ/cm^2 becomes insensitive to the total implanted O dose. Moreover, for fixed implanted O content, we observe an increase in the bandgap as the PLM energy fluence increases. This indicates that for high O content, less O is incorporated into the Te sublattice as the O^+-implanted CdTe samples are exposed to laser pulses with higher energy fluences.

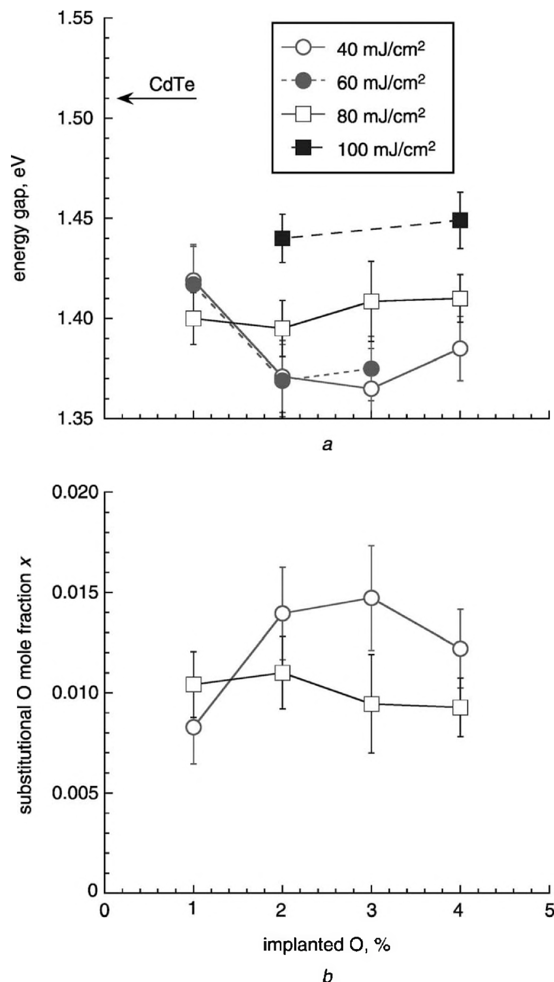

Fig. 3 *Bandgap energies and 'active' O mole fractions incorporated in the Te sublattice calculated according to the band anticrossing model of CdO_xTe_{1-x} alloys formed by O^+-implantation in CdTe followed by PLM with laser energy fluence 40–100 mJ/cm² as a function of implanted O^+ concentration*

This can be understood since increasing the energy fluence increases the melt depth in the sample and, consequently, also prolongs the duration of the melt/crystallisation process, driving the system closer to the equilibrium state. For CdTe implanted with 1–4% O and irradiated with energy fluence greater than 150 mJ/cm², no bandgap reduction was detected. This is consistent with the reported ablation threshold of ~0.12 J/cm² for CdTe using a 248-nm KrF laser pulse [25].

The amount of O incorporated into the Te sublattice in CdO_xTe_{1-x} HMAs can be determined using the band anticrossing (BAC) model (1). The location of the O level $E_O \approx E_V + 1.9$ eV in CdTe was determined from the location of E_O in ZnTe [26] and the known band offsets between ZnTe and CdTe. In the case of II–VI alloys, the matrix element C_{OM} was measured in $ZnSe_xTe_{1-x}$ and $ZnSe_yTe_{1-y}$ HMAs to be 1 eV [2]. In a recent report, Shan *et al.* studied the composition and pressure dependence of the electronic band structure of ZnO_xSe_{1-x} alloys grown by molecular beam epitaxy [14]. By fitting the optical transitions with the BAC model, they found that the interaction parameter $C_{OM} = 1.8 \pm 0.3$ eV for ZnO_xSe_{1-x}. In this work C_{OM} cannot be determined independently because a precise measurement of the fraction of O on the Te sublattice (i.e. x) is not possible. It is, however, believed that the magnitude of this matrix element depends on the electronegativity difference between the matrix anion elements [1]. From the dependence of the C_{OM} in the various II–VI HMA systems on the anion electronegativity difference, we make the reasonable assumption that $C_{OM} \approx 2.2$ eV in II–O–Te alloys. Notice that this C_{OM} is much smaller than the value (3.5 eV) we used in our previous work [15, 27]. This previous high value of C_{OM} was extrapolated from the matrix elements C_{NM} in III–N–V HMAs (GaN_xAs_{1-x} and InN_xP_{1-x}) and therefore may not apply in II–O–VI systems.

Using the estimated C_{OM} value of 2.2 eV and (1) we calculated the 'active' O mole fractions incorporated into the Te sublattice for CdO_xTe_{1-x} HMAs using a laser fluence of 40 and 80 mJ/cm² as a function of implanted O concentration. The results are shown in Fig. 3*b*. The x values shown in Fig. 3 reveal that for the lower implanted O^+ concentration of 1% the O activation efficiency is close to 100%. Moreover, the kinetic limit of solubility of O in CdTe for PLM at 40 mJ/cm² is ~0.015. For a PLM fluence of 80 mJ/cm² this limit decreases to ~0.01 because of the prolonged melt/crystallisation duration. This is in agreement with our previous report on the synthesis of GaN_xAs_{1-x}, where we found that increasing the energy fluence results in a decrease in the bandgap reduction and correspondingly a decrease in the amount of incorporated N [19].

We have also studied the thermal stability of the CdO_xTe_{1-x} alloys formed by implantation and PLM by subjecting the alloy to RTA for 10 s in the temperature range 300–500°C. We observe a reduction in the energy shift of the fundamental gap at RTA temperature higher than 300°C. This again suggests that the Cd–O bonds are relatively weak and these CdO_xTe_{1-x} alloys are thermally unstable. At an RTA temperature of 400°C, only the original E_M transition is observed. This may reflect that most of the implanted O atoms that resided in the Te sites after PLM diffused out of the Te sites, possibly forming O bubbles when subjected to the RTA process.

3.2 II–O–VI alloys with E_O below the conduction band

The effect of Mn on O incorporation is investigated in CdTe. Figure 4 shows PR spectra of two 4% O^+-implanted $Cd_{1-y}Mn_yTe$ samples with $y = 0$ and 0.4, after PLM. PR spectra of the original $Cd_{1-y}Mn_yTe$ substrates

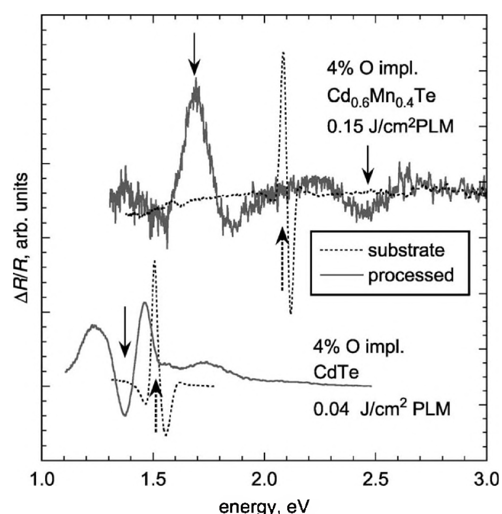

Fig. 4 *PR spectra of O^+-implanted $Cd_{1-y}Mn_yTe$ samples with $y = 0$ and $y = 0.4$ after PLM*

PR spectra of the original $Cd_{1-y}Mn_yTe$ substrates are also shown for comparison

are also shown for comparison. While only a relatively small reduction in the bandgap ($\sim$130 meV) is visible for the CdO_xTe_{1-x} layer, with $x \sim 0.012$, a large bandgap reduction of $\sim$400 meV is observed for the $Cd_{0.6}Mn_{0.4}O_xTe_{1-x}$ layer. Using the same value of $C_{OM} = 2.2$ eV, x is estimated to be 0.029. This clearly shows that Mn leads to increased incorporation of substitutional O on the Te sublattice of CdTe because of the formation of relatively strong Mn–O bonds [15].

We also note that E_O for a $Cd_{0.6}Mn_{0.4}Te$ crystal is at 2.06 eV, while the fundamental bandgap transition E_M is at 2.10 eV, corresponding to the case when E_O is below the conduction band minimum of the host (Fig. 1*b*). It is expected that the E_+ sub-band states attain more of the extended-like character and therefore optical transition from the valence band to E_+ is stronger. Indeed, another transition corresponding to the E_+ transition for the $Cd_{0.6}Mn_{0.4}O_xTe_{1-x}$ is observed at 2.45 eV in Fig. 4. Calculation based on the BAC model for $Cd_{0.6}Mn_{0.4}O_xTe_{1-x}$ with $x = 0.029$ yields $E_+ = 2.46$, in perfect agreement with the PR measurement.

It is worth mentioning that RTA processing after O^+-implantation in $Cd_{0.6}Mn_{0.4}Te$ results in a bandgap reduction of $\sim$130 meV. This corresponds to a $Cd_{0.6}Mn_{0.4}O_xTe_{1-x}$ alloy with O content $x \sim 0.0025$. PLM of the same O^+-implanted $Cd_{0.6}Mn_{0.4}Te$ sample results in more than an order of magnitude improvement of O incorporation to $x \sim 0.029$. This high O activation efficiency is achieved due to the extremely short melt duration ($\sim$200 ns) and regrowth process that promotes O substitution in the Te sublattice and inhibits the formation of oxygen-related voids.

The $Zn_{1-y}Mn_yTe$ alloys represent another interesting case in which the localised oxygen level lies well below the conduction band minimum for the whole Mn composition range (>200 meV). Figure 5*a* shows PR spectra from a $Zn_{0.88}Mn_{0.12}Te$ substrate and two $Zn_{0.88}Mn_{0.12}Te$ samples implanted with 3.3% O followed by PLM with laser energy fluence of 0.15 and 0.3 J/cm^2. Two optical transitions in the vicinity of $\sim$1.8 and 2.6 eV are clearly observed from the O^+-implanted samples after PLM. These transitions occur at energies distinctly different from the fundamental bandgap transition at $E_M = 2.32$ eV of the $Zn_{0.88}Mn_{0.12}Te$ matrix. These transitions can be attributed to transitions from the valence band to the two conduction sub-bands, E_+ ($\sim$2.6 eV) and E_- ($\sim$1.8 eV) formed as a result of the hybridisation of the localised O states and the extended conduction band states of ZnMnTe. The strong photomodulated transition signals indicate the extended nature of these electronic states and the substantial oscillator strength for the transitions. We point out that no optical transition is observed for the implanted samples with PLM fluence lower than 0.04 J/cm^2, while distinct E_+ and E_- transitions are observed for samples PLM at 0.08 J/cm^2. This indicates that the melting threshold for ZnMnTe is between 0.04 and 0.08 J/cm^2 under the current PLM conditions.

The substitutional mole fractions of O for the $Zn_{0.88}Mn_{0.12}O_xTe_{1-x}$ layers synthesised by ion implantation and PLM shown in Fig. 5*a* are calculated using the BAC model with the assumed value of $C_{OM} = 2.2$ eV. For the sample irradiated with 0.15 and 0.3 J/cm^2, x is estimated to be $\sim$0.024 and 0.018, respectively. The calculated energy band structure (left panel) and density of states (right panel) for the 0.15 J/cm^2 synthesised $Zn_{0.88}Mn_{0.12}O_xTe_{1-x}$ (with $x \sim 0.024$) are shown in Fig. 5*b*. A narrow band, E_- of O-derived extended states is separated from the conduction band by about 0.7 eV. The three possible optical transitions are indicated in the left panel.

The energy positions of E_- and E_+ for the $Zn_{0.88}Mn_{0.12}O_xTe_{1-x}$ alloys with different x are plotted in Fig. 6. Data taken from samples implanted with different concentrations of O (1.65, 2.2 and 4.4%) as well as PLM

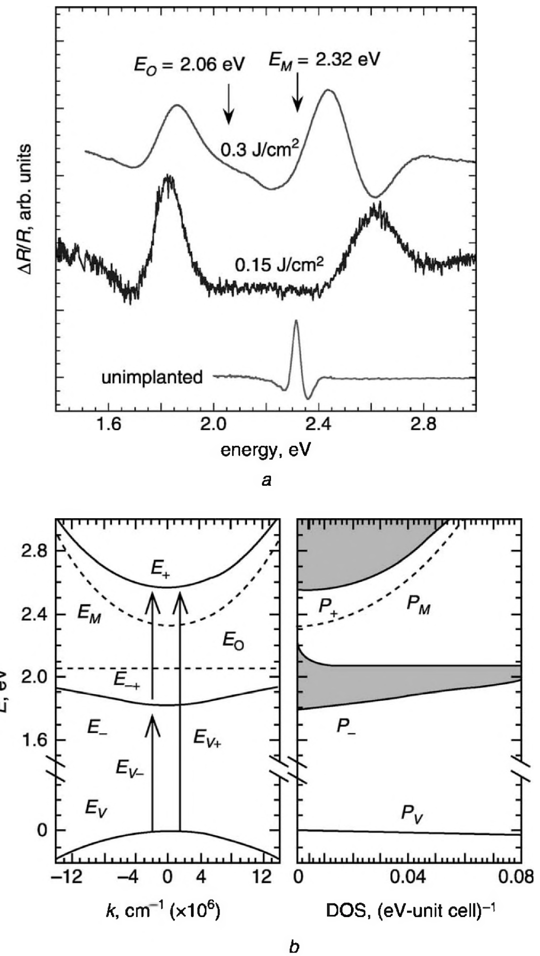

Fig. 5 *PR spectra and calculated band structure and density of states for O^+-implanted $Zn_{0.88}Mn_{0.12}Te$*

a PR spectra obtained from $Zn_{0.88}Mn_{0.12}Te$ samples as-grown and implanted with 3.3% O^+ followed by PLM with energy fluences of 0.15 and 0.3 J/cm^2

b Calculated energy band structure (left panel) and density of states (right panel) for 0.15 J/cm^2 synthesised $Zn_{0.88}Mn_{0.12}O_xTe_{1-x}$ (with $x \sim 0.023$) The three possible optical transitions are indicated in the left panel

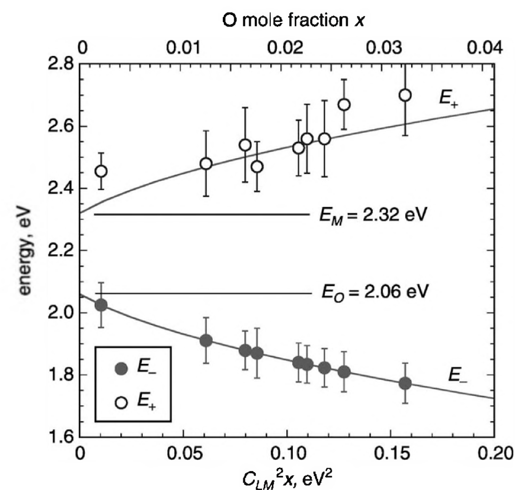

Fig. 6 *Energy positions of E_- and E_+ for $Zn_{0.88}Mn_{0.12}O_xTe_{1-x}$ alloys plotted against O mole fraction x*

Values of E_- and E_+ calculated according to the band anticrossing model are plotted as solid lines

with different energy fluences are also plotted in Fig. 6. We note in Fig. 6 that x decreases with increasing energy fluence beyond $\sim 0.08\,J/cm^2$, similar to the case of CdO_xTe_{1-x} alloys, possibly due to the longer melt duration and/or dilution through the deeper melt depth. The energy positions of the two transitions, as predicted by the BAC model, are also plotted as solid lines. Given the broader linewidths of the E_+ transitions, they agree reasonably well with the calculated values for samples with various O mole fractions.

The effects of applied pressure on the E_- transition in the $Zn_{0.88}Mn_{0.12}O_xTe_{1-x}$ samples were studied in order to verify the origin of the E_- sub-band. The energy positions of the E_- transition in the sample treated by PLM with a laser energy fluence of $0.3\,J/cm^2$ have been measured as a function of applied hydrostatic pressure at room temperature. The results are shown in Fig. 7, along with the measured pressure dependence of the bandgap of $Zn_{0.88}Mn_{0.12}Te$. The room-temperature energy E_+ at atmospheric pressure is also shown in the Figure. The inset shows a typical photomodulated transmission (PT) spectrum recorded at high pressures (4.7 kbar). The broad PT feature on the lower-energy side corresponds to the E_- transition and the narrow PT feature (E_g^{ZnMnTe}) on the higher-energy side is the transition associated with the fundamental bandgap of the $Zn_{0.88}Mn_{0.12}Te$ substrate.

By fitting the experimental data, represented by the open circle in Fig. 7, with the linear function we obtain the value of $dE_g/dP = 8.5\,meV/kbar$ for the coefficient of the energy gap of $Zn_{0.88}Mn_{0.12}Te$. Notice that the pressure-induced energy shift of the E_- transition of $Zn_{0.88}Mn_{0.12}O_xTe_{1-x}$ is much weaker (initial slope $\approx 2\,meV/kbar$) and nonlinear as compared to the change of the direct bandgap of $Zn_{0.88}Mn_{0.12}Te$. The weak pressure dependence of the E_- transition can be fully understood using the BAC model. The fact that E_- is located much closer to the energy level of the localised O states gives its wavefunction a pronounced O-like character. The solid lines through the experimental data in Fig. 7 are the calculated pressure dependencies of E_- and E_+ transitions using (1). The best fits to the data yield the energy position of the O level (relative to the top of the valence band) $E_O = E_V + 2.0 \pm 0.1\,eV$ at atmospheric pressure with a pressure dependence of $0.6 \pm 0.1\,meV/kbar$. It is clear from the Figure that the pressure dependence of E_- is slightly stronger than that of the O level as expected

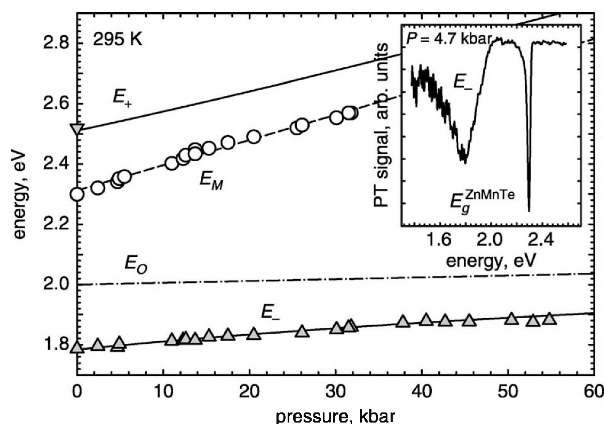

Fig. 7 *Effect of pressure on energy position of the E_- band edge of a $Zn_{0.88}Mn_{0.12}O_xTe_{1-x}$ sample (triangles)*

The change of bandgap of the $Zn_{0.88}Mn_{0.12}Te$ substrate with pressure is also displayed (○). The solid lines are theoretical fitting results; the dashed-dotted line is the location of E_O relative to the top of the valence band. The inset shows a typical photomodulated transmission (PT) spectrum of $Zn_{0.88}Mn_{0.12}O_xTe_{1-x}$ under pressure

from the admixture of extended conduction-band Γ_C states of the matrix to the E_- band-edge states. However, the much weaker pressure dependence of E_- as compared to that of the conduction-band Γ_C edge indicates the predominantly O-like nature of the E_- sub-band.

We point out that similar behaviour of the E_- sub-band edge under applied pressure was previously observed in GaN_xAs_{1-x} at the pressures high enough to shift the Γ conduction-band edge of the GaAs matrix above the localised N level [1–3]. Although it can only be explained by the BAC model as a pressure-induced transformation of the nature of the E_- sub-band from an extended to highly localised state GaN_xAs_{1-x}, the pressure dependence of E_- conduction-band edge along with the origin of the E_+ transitions, as well as its pressure dependence, have been a subject of debate due to the complexity of the conduction band structure of GaAs, the close proximity of the localised N level to the L conduction-band edges in particular. Here the $Zn_{1-y}Mn_yO_xTe_{1-x}$ system serves well as a test case for the BAC model since the conduction band L and X edges are located far away from the Γ edge (>1.0 eV) in $Zn_{1-y}Mn_yTe$. The much simpler band structure makes it much easier to directly evidence that E_- and E_+ transitions are the results of a band anticrossing interaction between the extended Γ conduction-band states and highly localised states in highly mismatched alloys.

3.3 Photovoltaic applications of II–O–VI HMAs

In addition to the unconventional conduction band structure the $Zn_{1-y}Mn_yO_xTe_{1-x}$ alloys represents an interesting case of a semiconductor with multiple direct gaps that has technological potential for photovoltaic applications. To date, the highest power conversion efficiency of ~33% has been achieved with multijunction solar cells based on standard semiconductor materials [28–30]. It was recognised over thirty years ago that the introduction of states in a semiconductor bandgap presents an alternative to multijunction designs for improving the power conversion efficiency of solar cells [31–33]. It was argued that deep impurity or defect states could play the role of the intermediate states for this purpose. Detailed theoretical calculations indicate that a single junction cell with one and two properly located bands of intermediate states (intermediate band solar cell IBSC) could achieve power conversion efficiencies up to 62% [32] and 71.7% [33], respectively. However, difficulties in controlling the incorporation of high concentrations of impurity or defect states have thwarted prior efforts to realise such materials [34].

As shown in the calculated band structure of the $Zn_{0.88}Mn_{0.12}O_xTe_{1-x}$ alloy in Fig. 5*b*, the three absorption edges: $E_+(k=0) - E_V(k=0) = 2.56\,eV$, $E_-(k=0) - E_V(k=0) = 1.83\,eV$ and $E_+(k=0) - E_-(k=0) = 0.73\,eV$ span much of the solar spectrum; thus these alloys are good candidates for the multiband semiconductors envisioned for high-efficiency IBSC. Calculations based on detailed balance theory [32, 33, 35] for this material yield an ideal power conversion efficiency of 45%. We note that even with this non-optimal bandgap configuration, the ideal power conversion efficiency is higher than that of any solar cell based on a single junction in a single-gap semiconductor and is comparable to the efficiency of a tandem cell (~55%) with two semiconductors of optimal bandgaps (0.7 and 1.5 eV) [32].

In order to optimise the solar cell performance, the three optical transition energies of the diluted II–VI oxide can be

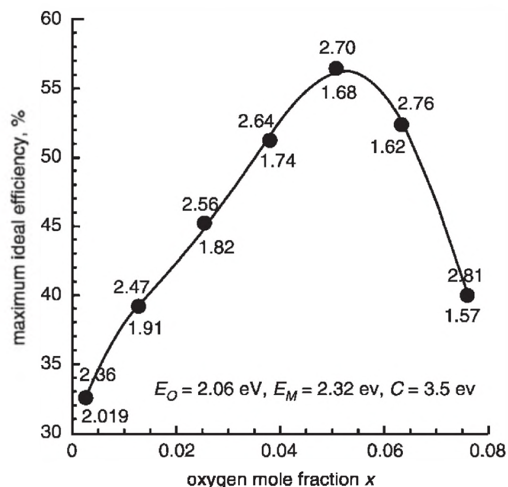

Fig. 8 *Calculated power conversion efficiency for a solar cell fabricated from a three-band $Zn_{0.88}Mn_{0.12}O_xTe_{1-x}$ alloy as a function of O content*

The solid line is an empirical polynomial fit of the calculated data

adjusted by varying the alloy composition. Figure 8 shows the calculated solar cell power conversion efficiency for a three-band $Zn_{0.88}Mn_{0.12}O_xTe_{1-x}$ alloy with varying O content. For example, increasing x in $Zn_{0.88}Mn_{0.12}O_xTe_{1-x}$ to slightly above 0.05 would increase the gap between E_+ and E_- to 1 eV and lead to a single-junction IBSC with an ideal efficiency of 56%. Also, it is noted that changing the Mn content or replacing Mn with Mg may provide another way to vary the band structure for further optimisation of solar cell performance.

4 Conclusions

We have carried out a systematic investigation of the synthesis and optical properties of the highly mismatched ternary and quaternary II–O–VI alloys. These diluted II–VI oxides are synthesised by O ion implantation in single-crystal II–VI substrates followed by pulsed laser melting. CdO_xTe_{1-x} thin films with x as high as 0.015, corresponding to a 150 meV reduction in the fundamental gap are formed. The much reduced bandgap corresponds to the transition from the valence band to the lower conduction sub-band that results from the anticrossing interaction between the localised O states and the extended conduction states of the matrix. Quaternary $Cd_{0.6}Mn_{0.4}O_xTe_{1-x}$ and $Zn_{0.88}Mn_{0.12}O_xTe_{1-x}$ HMAs were also synthesised using O^+-implantation and PLM with the mole fraction of incorporated O as high as 0.03. These materials represent the situation where the localised O level lies below the conduction-band edge of the matrix. Optical transitions corresponding to both the lower (E_-) and upper (E_+) conduction sub-bands are clearly observed in these quaternary diluted II–VI oxides, in good agreement with the BAC model. The weak pressure dependence of the E_- transition confirms the more localised nature of this band. These alloys have a three-band structure making them suitable for testing the theoretical predictions of the highly efficient intermediate-band solar cell concept. Theoretical ideal efficiency for IBSC using the $Zn_{0.88}Mn_{0.12}O_xTe_{1-x}$ HMAs is calculated to be 56%. We also point out that other diluted II–VI oxide materials that have a multiband configuration and may be possible candidates for the IBSC include the quaternary $Cd_{1-y}Zn_yO_xTe_{1-x}$ with $y > 0.7$ and $Cd_{1-y}Mn_yO_xTe_{1-x}$ with $y > 0.4$.

5 Acknowledgments

This work was supported by the Director, Office of Science, Office of Basic Energy Sciences, Division of Materials Sciences and Engineering, of the U.S. Department of Energy under Contract No. DE-AC03-76SF00098.

6 References

1 Shan, W., Walukiewicz, W., Ager, J.W., III, Haller, E.E., Geisz, J.F., Friedman, D.J., Olson, J.M., and Kurtz, S.R.: 'Band anticrossing in GaInNAs alloys', *Phys. Rev. Lett.*, 1999, **82**, pp. 1221–1224
2 Walukiewicz, W., Shan, W., Yu, K.M., Ager, J.W., III, Haller, E.E., Miotlowski, I., Seong, M., Alawadhi, J.H., and Ramdas, A.K.: 'Interaction of localized electronic states with the conduction band: band anticrossing in II–VI semiconductor ternaries', *Phys. Rev. Lett.*, 2000, **85**, pp. 1552–1555
3 Wu, J., Shan, W., and Walukiewicz, W.: 'Band anticrossing in highly mismatched III–V semiconductor alloys', *Semicond. Sci. Technol.*, 2002, **17**, pp. 860–869
4 O'Reilly, E.P., Lindsay, A., Tomic, S., and Kamal-Saadi, M.: 'Tight-binding and k·p models for the electronic structure of Ga(In)NAs and related alloys', *Semicond. Sci. Technol.*, 2002, **17**, pp. 870–879
5 'Special issue on III–N–V semiconductor alloys'. *Semicond. Sci. Technol.*, 2002, **17** (8) pp. 741–906
6 Skierbiszewski, C., Perlin, P., Wišniewski, P., Knap, W., Suski, T., Walukiewicz, W., Shan, W., Yu, K.M., Ager, J.W., Haller, E.E., Geisz, J.F., and Olson, J.M.: 'Large, nitrogen-induced increase of the electron effective mass in $In_yGa_{1-y}N_xAs_{1-x}$', *Appl. Phys. Lett.*, 2000, **76**, pp. 2409–2411
7 Yu, K.M., Walukiewicz, W., Shan, W., Ager, J.W., III, Wu, J., Haller, E.E., Geisz, J.F., Friedman, D.J., Olson, J.M., and Kurtz, S.R.: 'Nitrogen-induced increase of the maximum electron concentration in group III–N–V alloys', *Phys. Rev. B, Condens. Matter*, 2000, **61**, pp. R13337–R13340
8 Yu, K.M., Walukiewicz, W., Shan, W., Wu, J., Ager, J.W., III, Haller, E.E., Geisz, J.F., and Ridgway, M.C.: 'Nitrogen-induced enhancement of the free electron concentration in sulfur implanted GaN_xAs_{1-x}', *Appl. Phys. Lett.*, 2000, **77**, pp. 2858–2860
9 Yu, K.M., Walukiewicz, W., Wu, J., Mars, D., Chamberlin, D.R., Scarpulla, M.A., Dubon, O.D., and Geisz, J.F.: 'Mutual passivation of electrically active and isovalent impurities', *Nature Mater.*, 2002, **1**, pp. 185–189
10 Wu, J., Yu, K.M., Walukiewicz, W., He, G., Haller, E.E., Mars, D.E., and Chamberlin, D.R.: 'Mutual passivation effects in Si-doped diluted $In_yGa_{1-y}As_{1-x}N_x$ alloys', *Phys. Rev. B, Condens. Matter Mater. Phys.*, 2003, **68**, pp. 195202-1–195202-9
11 Yu, K.M., Walukiewicz, W., Wu, J., Shan, W., Beeman, J., Scarpulla, M.A., Dubon, O.D., Ridgway, M.C., Mars, D.E., and Chamberlin, D.R.: 'Mutual passivation of group IV donors and nitrogen in diluted GaN_xAs_{1-x} alloys', *Appl. Phys. Lett.*, 2003, **83**, pp. 2844–2846
12 Hong, Y., Nishikawa, G.A., and Tu, C.W.: 'Effect of nitrogen on the optical and transport properties of $Ga_{0.48}In_{0.52}N_yP_{1-y}$ grown on GaAs(001) substrates', *Appl. Phys. Lett.*, 2003, **83**, p. 5446–5448
13 Nabetani, Y., Mukawa, T., Ito, Y., Kato, T., and Matsumoto, T.: 'MBE growth and optical properties of ZnSeO', *Mater. Res. Soc. Symp. Proc.*, 2003, **744**, p. M3.4
14 Shan, W., Walukiewicz, W., Ager, J.W., III, Yu, K.M., Haller, E.E., Nabetani, Y., Mukawa, T., Ito, Y., and Matsumoto, T.: 'Effect of oxygen on the electronic band structure in ZnO_xSe_{1-x} alloys', *Appl. Phys. Lett.*, 2003, **83**, pp. 299–301
15 Yu, K.M., Walukiewicz, W., Wu, J., Beeman, J.W., Ager, J.W., Haller, E.E., Miotkowski, I., Ramdas, A.K., and Becla, P.: 'Band anticrossing in group $II-O_x-VI_{1-x}$ highly mismatched alloys: $Cd_{1-y}Mn_yO_xTe_{1-x}$ quaternaries synthesized by O ion implantation', *Appl. Phys. Lett.*, 2002, **80**, pp. 1571–1573
16 White, C.W., and Peercy, P.S. (Eds.): 'Laser and electron beam processing of materials' (Academic Press, New York, 1980)
17 Poate, J.M., and Mayer, J.W. (Eds.): 'Laser annealing of semiconductors' (Academic Press, New York, 1982), p. 385
18 Yu, K.M., Walukiewicz, W., Beeman, J.W., Scarpulla, M.A., Dubon, O.D., Pillai, M.R., and Aziz, M.: 'Enhanced nitrogen incorporation by pulsed laser annealing of GaN_xAs_{1-x} formed by N ion implantation', *Appl. Phys. Lett.*, 2002, **80**, pp. 3958–3960
19 Yu, K.M., Walukiewicz, W., Scarpulla, M.A., Dubon, O.D., Jasinski, J., Liliental-Weber, Z., Wu, J., Beeman, J.W., Pillai, M.R., and Aziz, M.J.: 'Synthesis of GaN_xAs_{1-x} thin films by pulsed laser melting and rapid thermal annealing of N^+-implanted GaAs', *J. Appl. Phys.*, 2003, **94**, pp. 1043–1049
20 Yu, K.M., Walukiewicz, W., Wu, J., Beeman, J.W., Ager, J.W., III, Haller, E.E., Shan, W., Xin, H.P., Tu, C.W., and Ridgway, M.C.: 'Formation of diluted III–V nitride thin films by N ion implantation', *J. Appl. Phys.*, 2001, **90**, pp. 2227–2234
21 Scarpulla, M.A., Yu, K.M., Monteiro Pillai, O.M., Ridgway, M.C., Aziz, M.J., and Dubon, O.D.: 'Ferromagnetic $Ga_{1-x}Mn_xAs$ produced

by ion implantation and pulsed-laser melting', *Appl. Phys. Lett.*, 2003, **82**, pp. 1251–1253
22 Pollak, F.H., and Shen, H.: 'Modulation spectroscopy of semiconductors: bulk/thin film, microstructures, surfaces/interfaces and devices', *Mater. Sci. Eng., R Rep.*, 1993, **10**, pp. 275–374
23 Aspnes, D.E.: 'Third-derivative modulation spectroscopy with low-field electroreflectance', *Surf. Sci.*, 1973, **37**, pp. 418–442
24 Jasinski, J., Yu, K.M., Walukiewicz, W., Liliental-Weber, Z., and Washburn, J.: 'Influence of microstructure on electrical properties of diluted GaN_xAs_{1-x} formed by nitrogen implantation', *Appl. Phys. Lett.*, 2001, **79**, pp. 931–933
25 Gnatyuk, V.A., Aoki, T., Gorodnychenko, O.S., and Hatanaka, Y.: 'Solid-liquid phase transitions in CdTe crystals under pulsed laser irradiation', *Appl. Phys. Lett.*, 2003, **83**, pp. 3074–3076
26 Seong, M.J., Alawadhi, H., Miotkowski, I., Ramdas, A.K., and Miotkowska, S.: 'Oxygen isoelectronic impurity in ZnS_xTe_{1-x}', *Phys. Rev. B, Condens. Matter*, 1999, **60**, pp. R16275–R16278
27 Yu, K.M., Walukiewicz, W., Wu, J., Shan, W., Beeman, J.W., Scarpulla, M.A., Dubon, O.D., and Becla, P.: 'Diluted II–VI oxide semiconductors with multiple band gaps', *Phys. Rev. Lett.*, 2003, **91**, pp. 246403/1–4
28 Chiang P.K., Ermer, J.H., Nishikawa, W.T., Krut, D.D., Joslin, D.E., Eldredge, J.W., Cavicchi, B.T., and Olson, J.M.: 'Experimental results of $GaInP_2$/GaAs/Ge triple junction cell development for space power systems'. Proc. 25th IEEE Photovoltaic Specialists Conf., Washington, DC, USA, 1996, pp. 183–186
29 Kurtz, S.R., Myers, D., and Olson, J.M.: 'Projected performance of three- and four-junction devices using GaAs and GaInP'. Proc. 26th IEEE Photovoltaic Specialists Conf., Anaheim, CA, USA, 1997, pp. 875–878
30 King, R.R., Colter, P.C., Joslin, D.E., Edmondson, K.M., Krut, D.D., Karam, N.H., and Kurtz, S.: 'High voltage, low-current GaInP/GaInP/GaAs/GaInNAs/Ge solar cells'. Proc. 29th IEEE Photovoltaic Specialists Conf., New Orleans, LA, USA, 2002, pp. 852–855
31 Wolf, M.: *Proc. IRE*, 1960, **48**, p. 1246
32 Luque, A., and Marti, A.: 'Increasing the efficiency of ideal solar cells by photon induced transitions at intermediate levels', *Phys. Rev. Lett.*, 1997, **78**, pp. 5014–5017
33 Brown, A.S., Green, M.A., and Corkish, R.P.: 'Limiting efficiency for a multi-band solar cell containing three and four bands', *Physica E*, 2002, **14**, pp. 121–125
34 Cuadra, L., Marti, A., and Luque, A.: 'Present status of intermediate band solar cell research', *Thin Solid Films*, 2004, **451–452**, pp. 593–599
35 Shockley, W., and Queisser, H.J.: 'Detailed balance limit of efficiency of *p-n* junction solar cells', *J. Appl. Phys.*, 1961, **32**, pp. 510–519